Progress Towards Electromagnetic Manipulation and Trapping of Micro-particles

A thesis submitted in partial fulfillment of the requirement
for the degree of Bachelor of Science with Honors in Physics from
William & Mary

by

Andrew J. Beling

Accepted for Honors

_____
Advisor: Prof. Seth Aubin

_____
Prof. Todd Averett

_____
Prof. Jonathan Frey

Williamsburg, VA
May 3, 2021

Progress Towards Electromagnetic Manipulation and Trapping of Micro-particles

A thesis submitted in partial fulfillment of the requirement
for the degree of Bachelor of Science with Honors in
Physics from the College of William and Mary in Virginia,

by

Andrew J. Beling

_____

Advisor: Prof. Seth Aubin

_____

Prof. Todd Averett

_____

Prof. Jonathan Frey

Williamsburg, Virginia
May 2021

Contents

Acknowledgments

List of Figures

List of Tables

Abstract

This thesis describes research to investigate the electromagnetic manipulation of microspheres and microrings. The work consists of three main thrusts: 1) the use of an electric field gradient to move dielectric microspheres, 2) the use of an AC magnetic field to move a conducting ring, and 3) the preparation of substrates for a microwave atom chip. The electrostatic movement of dielectric polyethylene microspheres was observed and recorded with a CCD imaging system. The microspheres were suspended in various liquids and placed on top of a microstrip transmission line, which consists of a conducting copper trace separated from a ground plate by an FR4 dielectric substrate. 5 kV was applied to the conducting trace. Some microspheres acted as weak field seekers and were repelled from the trace, as predicted by theoretical calculations, while others acted as strong field seekers and were attracted to the trace. Electromagnetic simulations generated using the software FEKO indicate that the dipole force experienced by the microspheres should be several orders of magnitude higher than experimentally observed. Further research is necessary to reconcile the difference between theoretical calculations and observed microsphere behavior, but it seems likely that competing electrokinetic effects impede the movement of microspheres. Several microrings were constructed and placed in the vicinity of an alternating magnetic field. Theoretical calculations were performed to estimate: a) the cutoff frequency at which microrings act inductively and b) the force experienced by microrings. No microring movement was observed in preliminary experiments, but further experiments were conducted to find the cutoff frequency using a multi-turn pickup coil and the magnetic field generated by a solenoid.

Chapter 1

Introduction

1.1 Objective

The objectives of this thesis are twofold. First: to achieve the electrostatic movement of a dielectric microsphere suspended in a dielectric fluid. Second: to use an AC magnetic field to push or pull a conducting microring. This thesis also provides a foundation for longer term investigation of these phenomena. By confirming the basic physics involved, the research discussed in this thesis aims towards several longer term goals, namely the manipulation and levitation of both microspheres and microrings using microwave near fields generated by various microstrip geometries printed on a microfabricated chip.

1.2 Background

Electromagnetic near-field minima can be used to trap both small dielectric particles and ultra-cold atoms, and therefore investigation in this area is of interest to the Aubin Lab [1]. Previously, William & Mary's Ultra-cold AMO Physics laboratory has used an optical dipole trap for ultra-cold atom trapping. Similar techniques involve the use of optical tweezers to trap dielectric microspheres [2]. Dielectric microspheres are trapped by the electric field, while atoms are trapped by the magnetic field.

However, at microwave and RF frequencies there is often a correspondence between the electric near-field minima and the magnetic near-field minima [1]. Therefore, dielectric microspheres can serve as a stand-in for ultra-cold atoms in a large scale version of an atom chip trap. If microspheres can be trapped by a large scale version of an atom chip when suspended in a dielectric liquid, then, in principle, the smaller scale version of the atom chip will be able to trap atoms. An example of an atom chip, similar to the ones used in W&M's Ultra-cold AMO Laboratory is shown in Fig. 1.1. There are also possible future microfluidic applications to be gleaned from these experiments. For example, it may prove useful to use electric or magnetic dipole forces to manipulate proteins in a liquid [3] [4] [5].
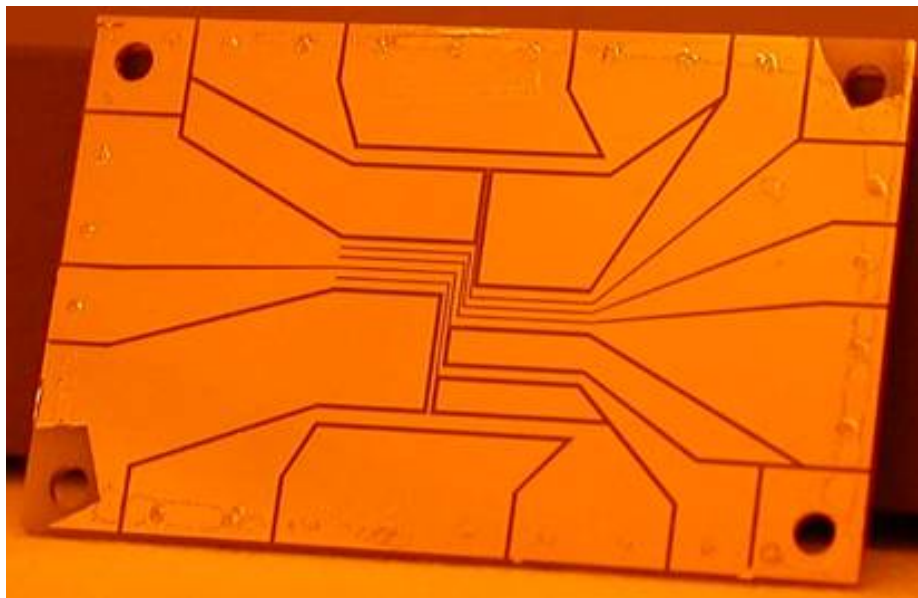
Figure 1.1: An atom chip consisting of gold wires on an AlN substrate. From the Thywissen group (Department of Physics, U. of Toronto Canada)

Earnshaw's theorem forbids electrostatic and magnetostatic maxima, but local minima are permitted (see [6], page 115). Microwave near-fields are largely expected to follow this theorem, meaning only weak-field seekers can be trapped. Dielectric

microspheres are strong-field seekers, but when embedded in a liquid with a higher dielectric constant they will act as weak-field seekers; conducting microrings will also act as weak magnetic field seekers for high frequencies [7]. Previous work in this area involved microwave simulations using the commercial software product FEKO, and found that a current running through two or three parallel microstrips will generate an electromagnetic field minimum that could be suitable for trapping a dielectric micro-particle [1].

This project has built on this foundation and sought to achieve the experimental objectives described above. The project had two principal phases. The first phase centered on attempting to achieve the electrostatic movement of dielectric microspheres and the attempted trapping of those microspheres. The second phase involved experiments aiming to move and levitate conducting microrings. Microwave electronics were initially planned to be used to translate microsphere traps, but this was unsuccessful. The experiments on trapping and manipulation of micro-particles also provide experience for an ongoing project in the Aubin Lab on trapping of ultra-cold atoms using microwave near fields on atom chips [7]. Indeed, the group has recently succeeded in trapping ultra-cold atoms with MHz frequency magnetic near fields. The work in this thesis also informs existing efforts to design and microfabricate a microwave atom chip. Additionally, the movement of microspheres (and hopefully microrings too) discussed in this thesis could serve as an informative demonstration of dipole forces as a supplement to an electricity and magnetism course.

1.3   Structure of Thesis

This thesis is structured as follows. Chapters 2, 3, and 4 cover the three primary thrusts of the research. Chapter 2 focuses on the electric manipulation of dielectric microspheres. In this chapter, I discuss the theory and physics underlying micro-

spheres and microstrip transmission lines, the experimental PCB apparatus, the 1:1 CCD imaging system, and the experimental results of these experiments. Chapter 3 covers the magnetic manipulation of a conducting loop; chapter 4 covers atom chip substrate development. Chapter 5 concludes the report and involves a discussion of the project's outlook and possible future planned experiments.

Chapter 2

Electric Manipulation of Dielectric Microspheres

In this chapter, I discuss the theory and physics of dielectric microspheres and microstrip transmission lines. I present several methods of approximating the force experienced by the microspheres and in section 2.2 I also introduce the experimental apparatus used to view microsphere movement. Finally, I present the results of these microsphere experiments in section 2.3.

2.1 Theory

The electrostatic portion of this project uses microstrip transmission lines to generate electric near fields. Microstrip transmission lines consist of conducting traces that are separated from a grounded plate by a dielectric substrate [8]. The strong gradient of the near field generated by these traces will generate forces in the plane perpendicular to the traces, and can be tuned such that the near field has a minimum in this plane [7]. A microsphere suspended in a liquid with a higher dielectric constant will seek this minimum, and if the gradient force is of similar size to the weight of the sphere, then the sphere could be suspended above the traces.

The force experienced by a spherical dielectric particle suspended in a dielectric

liquid in a spatially dependent electric field is as follows [6] [9]:

$$\vec{F} = (\vec{p} \cdot \vec{\nabla})\vec{E} = (4\pi r^3 \epsilon_0 \epsilon_b \frac{\epsilon_a - \epsilon_b}{\epsilon_b + 2\epsilon_a}\vec{E} \cdot \vec{\nabla})\vec{E}, \tag{2.1}$$

where $\vec{p}$ is the dipole moment of the microsphere, ϵ_b is the dielectric constant of the liquid, ϵ_a is the dielectric constant of the microsphere, and r is the radius of the microsphere. Note that if the dielectric constant of the embedded microsphere is less than the dielectric constant of the liquid, than the microsphere will experience a force in the opposite direction of $\vec{E}$. In other words, the sphere becomes a weak-field seeker. It follows from Eq. 2.1 that the potential energy of a dielectric microsphere embedded in a dielectric liquid is

$$U = -\frac{1}{2}(4\pi r^3 \epsilon_0 \epsilon_b \frac{\epsilon_a - \epsilon_b}{\epsilon_b + 2\epsilon_a}E^2). \tag{2.2}$$

From the form of this equation, it becomes clear that if $\epsilon_a > \epsilon_b$, then the energy of the dielectric particle is minimized at large values of E, making the microsphere a strong field seeker. Conversely, if $\epsilon_a < \epsilon_b$, then the dielectric particle will seek the minimum of the electric field, E, to minimize its potential energy.

What follows is an approximate calculation of the force experienced by a polystyrene dielectric microsphere suspended in water on top of a microstrip transmission line. The dimensions used in this calculation correspond to the dimensions used in FEKO simulations (discussed in subsection 2.2.1) and the dimensions of the real microstrip transmission lines tested in section 2.3. If the copper trace (0.75 mm wide) on a dielectric substrate is held at 100 V and is 0.397 mm away from the ground plane on the bottom side of the substrate, then the electric field in the vicinity of the trace will be on the order of 250 kV/m. If we assume that this electric field drops off to 0 V over 6 mm, then the gradient of the electric field will be on the order of 4-5$\times 10^7$ V/m^2. Therefore, the dipole force will accelerate polystyrene particles at about 11-12 m/s^2. This preliminary calculation shows that the transverse trapping acceleration

is around the same order of magnitude as gravitational acceleration. Note that this acceleration depends only on the density of the microsphere material (1.06 g/cm^3 for polystyrene), and not on the radius of the particle:

$$\vec{a} = \frac{\vec{F}}{m} = \left(\frac{3}{\rho}\epsilon_0\epsilon_b\frac{\epsilon_a - \epsilon_b}{\epsilon_b + 2\epsilon_a}\vec{E}\cdot\vec{\nabla}\right)\vec{E}. \tag{2.3}$$

We can calculate a more precise force using the method of images. In this method, the conducting ground copper plane is replaced by a mirror image microstrip trace where the polarity of charge is flipped. Similarly, a reflected dielectric is generated in the image method directly opposite the real dielectric. In the case of AC currents, current will flow in the opposite direction of the real microstrip trace. The method of images for a microstrip trace is shown below in Fig. 2.1 [1].
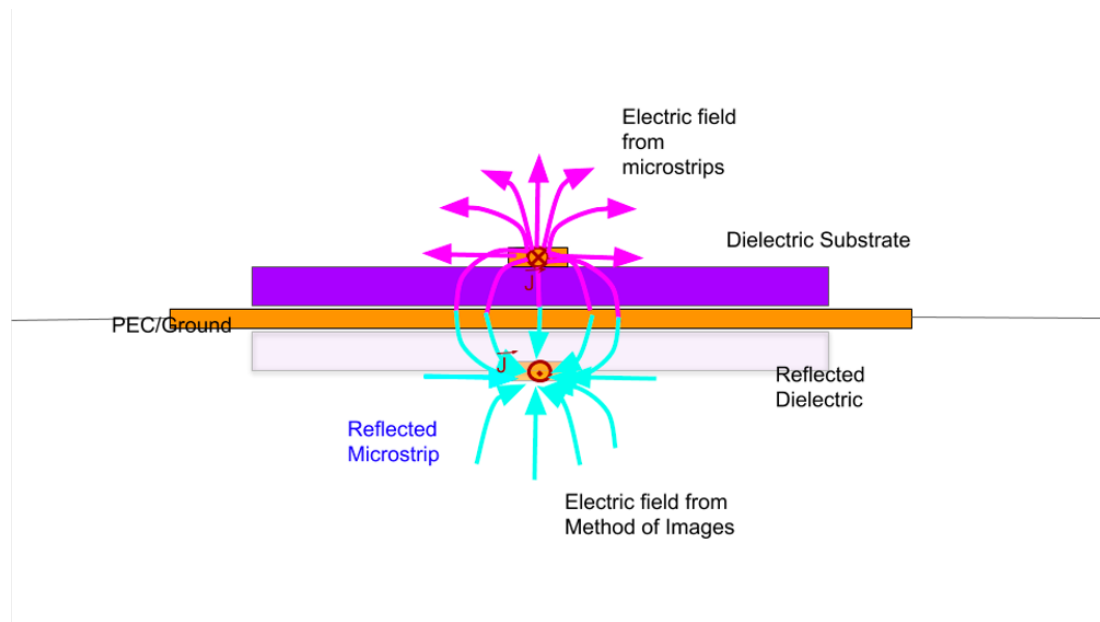
Figure 2.1: Electric field generated by a microstrip transmission line. (Image from C. Lewelling Senior Thesis, W&M, 2018)

The calculation of the microstrip transmission line electric field can be performed analytically using this method, but the expression is lengthy [10]. Instead, we use the

commercial electromagnetic simulation software FEKO to numerically approximate the electric field, as discussed in section 2.2.

2.2 Experimental Apparatus

2.2.1 FEKO Simulations

Further investigation of the dielectric force experienced by a suspended microsphere was conducted to provide a more concrete estimate of the magnitude of force expected. A model of a microstrip transmission line consisting of a copper trace with a width of 0.75 mm and a dielectric FR4 substrate with a width of 397 μm was simulated in FEKO to determine the electric field. 1 V was applied to the copper trace in the simulation, and the resultant electric field was scaled up by a factor of 3000 to simulated an applied voltage of 3000 V. The value of 3 kV was chosen because it was the highest output of one of the power supplies used. Next, this electric field was inserted into Eq. 2.1 and used to plot the dielectric particle's acceleration as a function of position. It was found that the dielectric force strength exceeded the force of gravity within 3 mm of the microstrip trace, as shown in Fig. 2.2. These simulations were conducted at microwave frequencies between 1 GHz and 9 GHz. These simulations do not exactly correlate with the electrostatic case, but they do provide a more concrete approximation of the expected force.
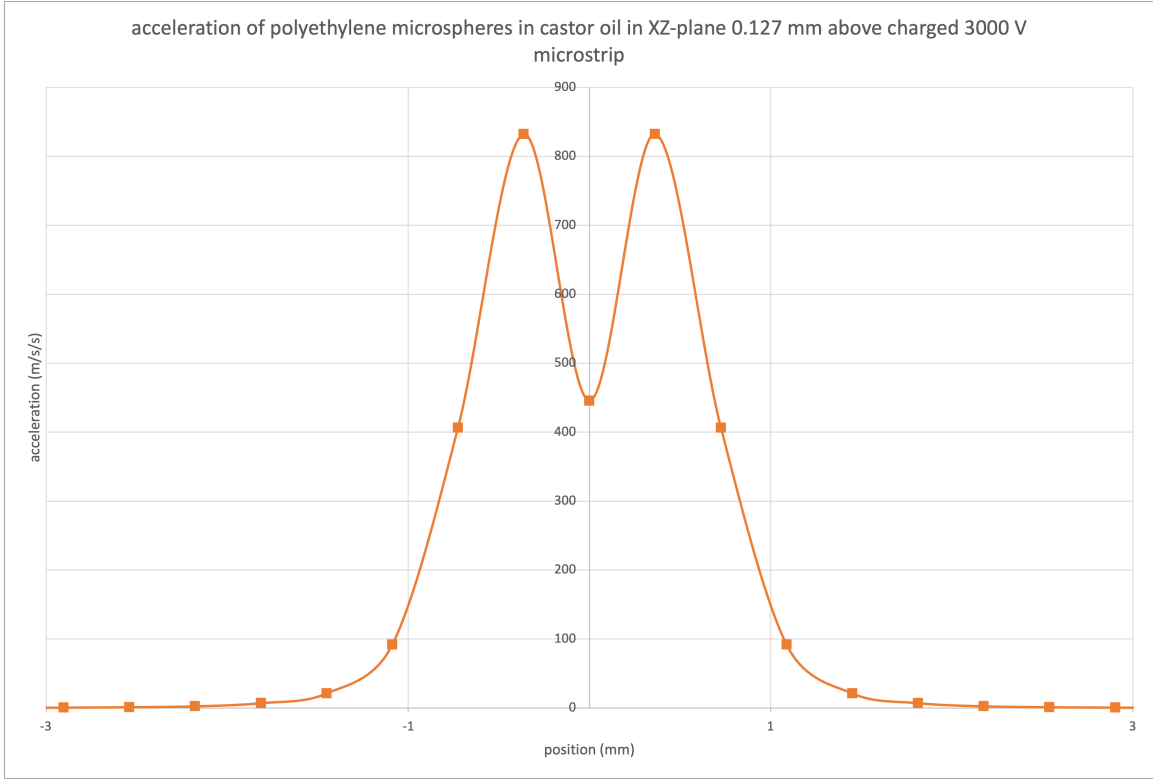
Figure 2.2: The acceleration of a polyethylene microsphere suspended in castor oil according to Eq. 2.1 applied to the electric field calculated using FEKO. The two large bumps in the graph are from the accumulation of charge at the edges of the trace due to the AC Skin effect. The electric field was simulated for an applied alternating current with a frequency of 1 GHz. For electrostatic experiments, this will not occur. The acceleration is plotted in a linear scale, with the max acceleration larger than 800 $\frac{m}{s^2}$ and the acceleration on the particle greater than 50 $\frac{m}{s^2}$ within 1 mm of the center of the conducting trace.

2.2.2 Microwave Force Simulation

This procedure was repeated for a lower voltage of 0.775 V. This voltage is the output from our 12 mW microwave amplifier system. Applying microwaves to the trace would allow us to translate the microspheres along the trace. However, the simulations showed that microspheres suspended in castor oil on the trace would experience a much smaller acceleration of less than 4×10^{-4} $\frac{m}{s^2}$ (see Fig. 2.3). This demonstrates that the force experienced by a microsphere in a microwave experiment

will be six orders of magnitude smaller than the force experienced by a microsphere in an electrostatic experiment.
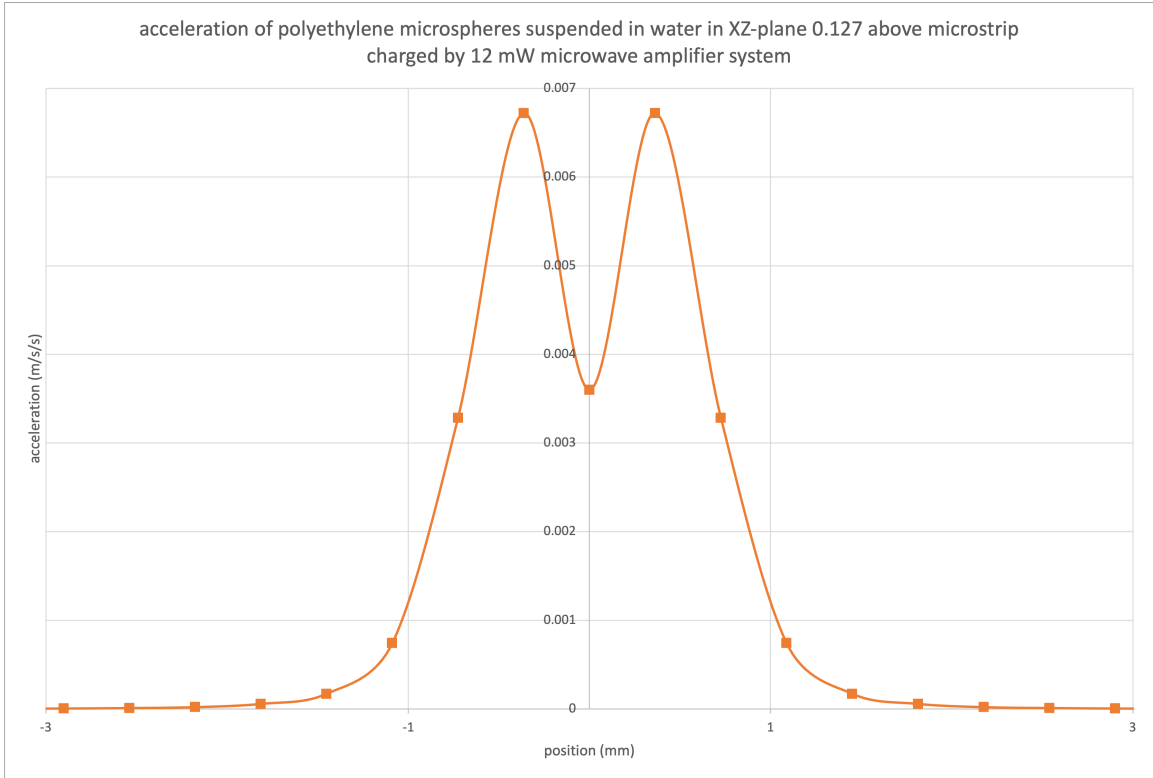
Figure 2.3: The acceleration of a polyethylene microsphere suspended in castor oil according to Eq. 2.1 applied to the electric field calculated using FEKO at a frequency of 1 GHz. In this case, the voltage is provided by a microwave amplifier. Acceleration does not exceed $4 \times 10^{-4} \ \frac{m}{s^2}$.

2.2.3 Experimental Design

Next, an existing microstrip transmission line was used to test the attraction and repulsion of various dielectric liquids and dielectric microspheres. These microsphere experiments are entirely electrostatic in nature; in section 2.1.2, we saw that our microwave amplifiers are unable to supply sufficient voltage to reach large forces. The microspheres used can be seen in Fig. 2.4.
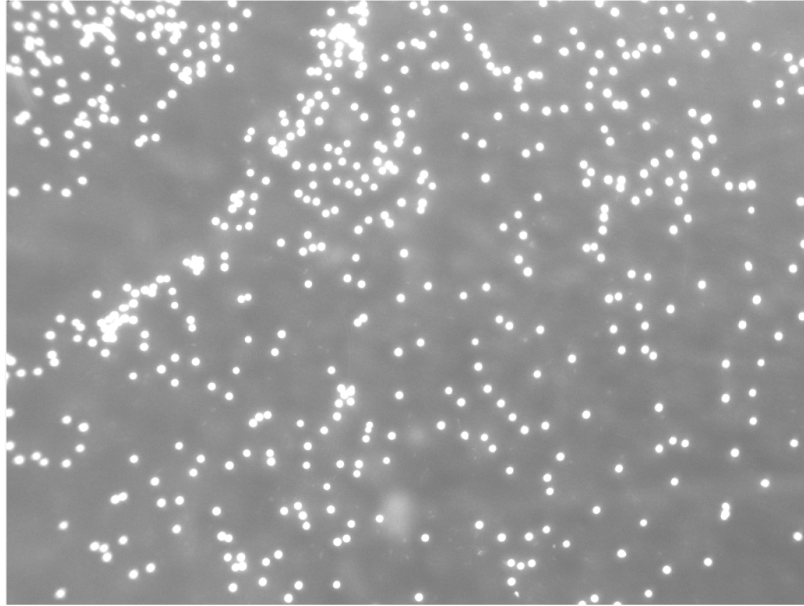
Figure 2.4: Image of 50 micrometer polyethylene microspheres taken with camera's Point Grey Fly Cap 2 software.

A series of experiments were undertaken to test the movement of drops of dielectric liquid and dielectric microspheres suspended in dielectric liquid. Liquids were confined to the microstrip trace by creating an elevated barrier with epoxy, resin, and hot glue. A 5 kV power supply was used to charge the conducting copper trace and to ground the copper plane. Image and video data were captured using a CCD camera with a 1:1 imaging system. This imaging system and the experimental setup are shown in Fig. 2.5.
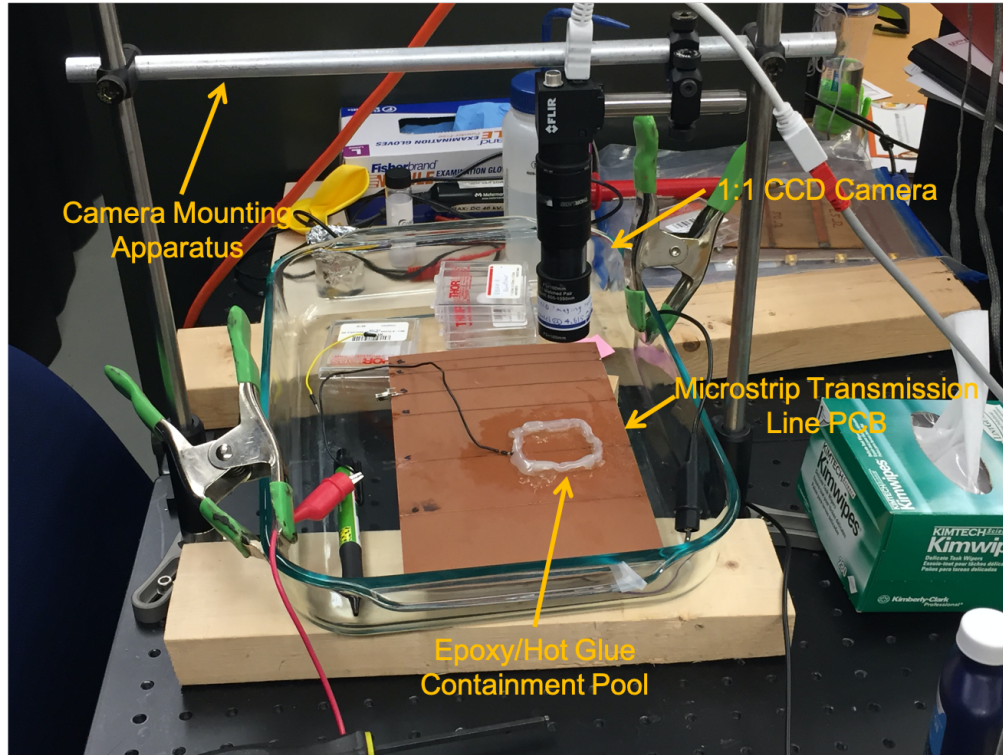
Figure 2.5: The experimental setup. The CCD camera is suspended by the mounting system 10.5 *cm* above the microstrip transmission line. A containment pool of epoxy and hot glue on the trace is used to confine the dielectric liquid.

2.2.4   Creation and Calibration of the CCD Imaging System

To properly visualize the movement of polyethylene microspheres with a diameter of 50 microns, a CCD camera and imaging platform was created and calibrated with the imaging of an electron beam. A 1:1 imaging system was constructed produce a CCD image where there is no magnification. In other words, the image distance and object distance (where the object is located roughly at the camera's focal length of 10.75 cm) are equal. Next, the camera's pixel density was experimentally determined by viewing a ruler on the camera's Point Grey Fly Cap 2 software's graphical user interface (GUI) and correlating the ruler's length with a pixel distance. The camera's resolution was found to be 4.615 pixels per micrometer with an aspect ration of 960

$\times$ 1280 pixels.
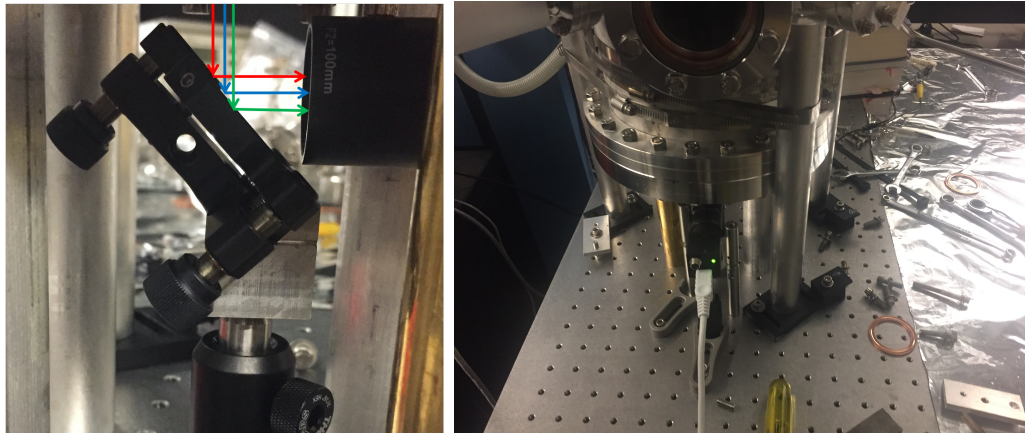
Figure 2.6: The electron beam and camera apparatus, viewed from the side (left image) and the front (right image, placeholder image). The 45 degree mirror redirects the field of view of the camera upwards to the phosphor plate and the electron beam.

A mounting system was constructed to hold the camera above the PCB at a height equal to the focal length of the camera, which was experimentally determined to be 10.75 cm. The calibration and viewing ability of the camera was tested in a separate project to view an electron beam in the Quantum Measurement Lab (Small Hall 232). In this separate calibration and testing experiment, an electron beam was directed onto a phosphor plate. The camera is focused onto this phosphor plate. When struck by electrons, the phosphor plate emits photons in the visible spectrum which can be viewed by the camera. This experimental setup is demonstrated in Fig. 2.6. The data from the beam image captured by the camera, shown in Fig. 2.7, was analyzed using Python, showing that the electron beam has a Gaussian shape (see Fig. 2.8), with a full width at half maximum of 67 pixels or 309 microns.

Figure 2.7: An image of the electron beam captured by the CCD imaging system. Brighter, higher intensity pixels show the location of the beam.
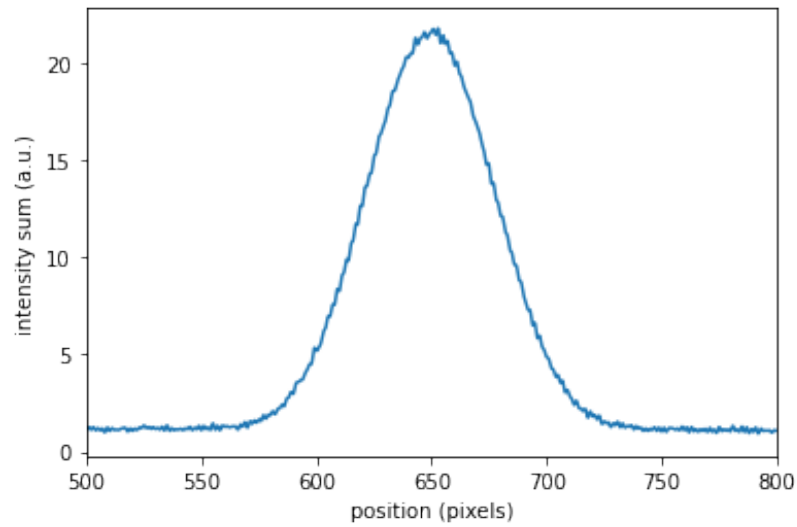
Figure 2.8: The Gaussian distribution produced when the image of the electron beam is analyzed. Image analysis is performed by summing up the intensity of the pixels in every row. The code written to analyze the electron beam intensity data and calculate the full width at half maximum of the beam is provided in Appendix A.

2.3   Experimental Results

The experiments conducted yielded behavior that did not align with theoretical calculations. Water, which should act as a strong-field seeker and therefore experience a strong force of attraction towards the charged microstrip, remained stationary in the vicinity of the microstrip transmission line. Likewise, polyethylene microspheres suspended in water did not act as weak-field seekers and instead remained stationary. Eq. 2.1 is only valid if both the dielectric liquid and the embedded microsphere are non-conducting [11]. These experiments were repeated with distilled and de-ionized water to minimize conduction, but the water remained stationary in both cases. Measurements with a multimeter showed a resistance of about $2{\times}10^6$ Ω in both cases.

Liquid	Dielectric constant	Conductor?
Water	78.4	Yes
Castor Oil	4.7	No
Soybean Oil	2.8	No
Acetone	20.7	Yes
Liquid Nitrogen	1.5	No

Table 2.1: Table of dielectric constants and conducting ability for several tested liquids.

Next, castor oil was used as the dielectric liquid since it is significantly less conductive than water. While castor oil has a lower dielectric constant than water (and therefore the micro-particles will experience less force), its dielectric constant is large compared to other non-conducting liquids (see Table 2.1). A grounded wire was also inserted into the castor oil to help dissipate excess charge and minimize any Coulombic effects. Small drops of castor oil were placed on the microstrip trace, which was set to 5 kV. The drops were repelled by the trace. This is peculiar, since castor oil should act as a strong field-seeker in air. Larger pools of castor oil exhibited the same behavior, and were repelled from the trace. The level of liquid above the trace

dropped as the liquid was parted. This same behavior was observed using soybean oil as the liquid medium, as shown in Fig. 2.9.
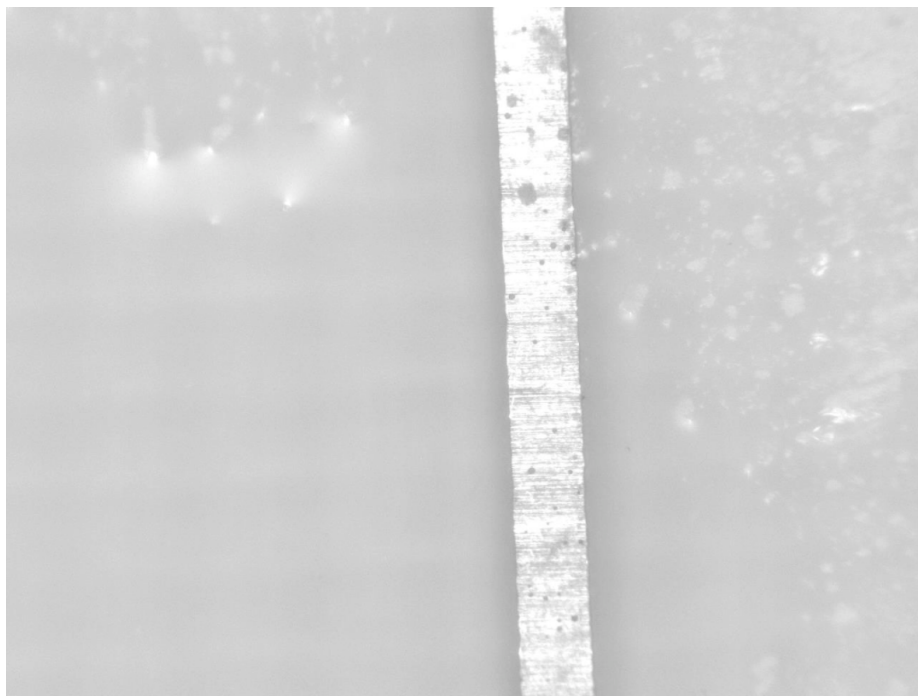
Figure 2.9: The movement of a drop of soybean oil away from the conducting microstrip trace when 5 kV is applied. When voltage is applied to the conducting trace in the center of the image, the surrounding oils is pushed away (see video).

Microspheres were suspended in the castor oil and the previous experiments were repeated. Finally, there was clear movement of the polyethylene microspheres when 5 kV was applied. Like with the castor oil, the microspheres were seen to move away from the trace. However, they can also be seen in Fig. 2.10 moving towards the trace before being repelled. It is possible that the microspheres are simply being pulled by the oil as it moves away from the trace.
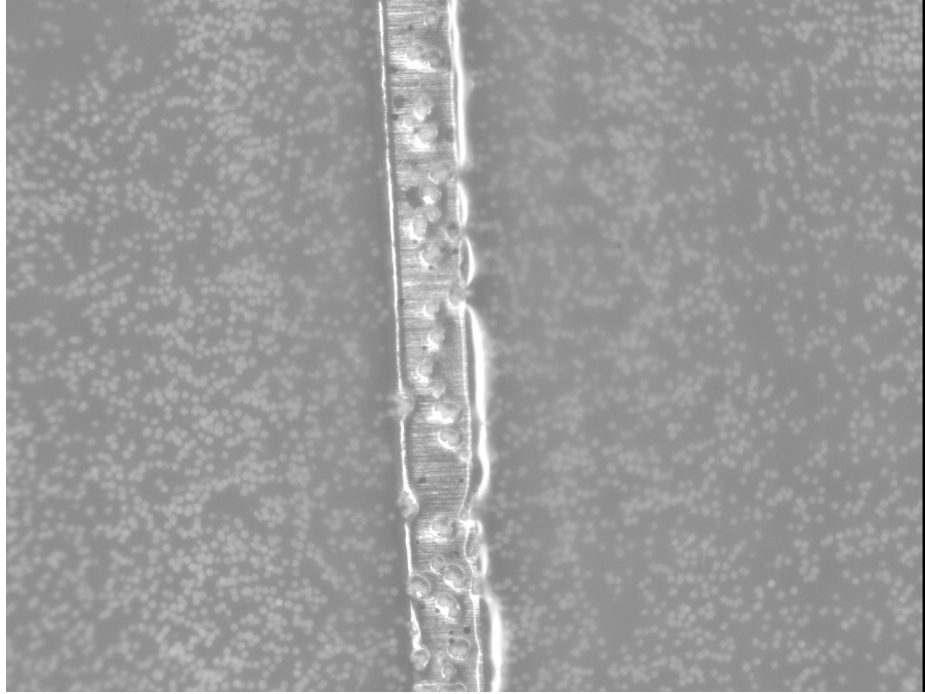
Figure 2.10: The movement of polyethylene microspheres in castor oil when 5 kV is applied to the conducting copper trace. The liquid level recedes from the trace as it is pushed away, acting as a weak field seeker. In the center of the image you can see the microstrip trace surrounded on both sides by 50 μm microspheres suspended in castor oil.

These experiments were repeated with a deeper layer of castor oil, as shown in Fig. 2.11. The same behavior of microspheres was observed. It is not clear exactly why experiment does not agree with theory; further investigation of the existing literature is needed.

Figure 2.11: The movement of polyethylene microspheres in a high level of castor oil when 5 kV is applied to the conducting copper trace. The liquid level recedes from the trace as it is pushed away, acting as a weak field seeker.

Based on the work of others [3] [12], there seem to be two probable explanations for the discrepancy. First, according to work by Nakano [3], at low frequencies (i.e. electrostatics), Eq. 2.1 is not the dominant force mechanism. Only at high frequencies is the force governed by the medium and particle permitivities. At low frequencies, the force is governed instead by the medium and particle conductivities. We also expect that the particle will change from a low field to a high field seeker as we go between the low frequency and high frequency regimes [3].

Secondly, there seem to be competing electrokinetic, hydrodynamic, and drag forces that oppose the dielectric force. The microspheres are not neutrally charged, so they will be affected by the ordinary Coulombic force. As they contact each other, microspheres will accumulate electrostatic charge on their surface [12]. This

is inevitable whenever any two objects come into contact. Moreover, environmental factors such as humidity can facilitate the transfer of charge. Groups of particles periodically gaining and losing charge may explain the wave like motion seen in the videos. Other experiments that have used the dielectric force for protein manipulation seem to use a minimum ∇E^2 value on the order of $1x10^{21}$ $\frac{V^2}{m^3}$ [4]. Currently, the microsphere experiment achieves a ∇E^2 value that is about 5 orders of magnitude lower. Future experiments will need smaller microstrip traces and/or higher voltages to achieve higher gradients. Additionally, it may prove prudent to move towards working with alternating currents.

Chapter 3

Magnetic Manipulation of a Conducting Loop

In this chapter, I discuss the magnetic portion of this thesis, where I try to use alternating currents and magnetic forces to move conducting microrings. The first section of this chapter will discuss microring theory and introduce the basic underlying physics. In this section, I explain the origin of the force on conducting microrings, calculate the expected microring cutoff frequency, and calculate the expected force on the microring. In section 3.2, I discuss the experimental apparatus and the results of the microring experiments.

3.1 Theory

The second portion of this project involves microrings. A microwave amplifier can be used to apply microwaves to the conducting trace, allowing translation of trapped microspheres. Additionally, PCBs with multi-trace configurations are expected to generate magnetic near-field minima in the plane above the traces [1]. This means that conducting microrings, which are expected to be dynamically diamagnetic for microwave frequencies, can be moved, translated, and even levitated with microwave near fields generated by microstrip transmission lines.

At high frequencies, the inductive reactance of a ring will be much larger than its resistance. According to Faraday's Law, a changing magnetic flux (Φ) through a conducting circuit induces an emf ($\mathcal{E}$) in that circuit. This emf drives a current in the circuit; this current's magnetic field will oppose the change in magnetic flux as shown below:

$$\mathcal{E} = \oint \vec{E} \cdot d\vec{l} = -\frac{d\Phi}{dt}. \tag{3.1}$$

If the resistance of the circuit dominates, then resultant forces will average out to zero. However, if the product of the self inductance and the current frequency (together known as the inductive reactance) is significantly larger than the resistance, then resultant repulsive forces will not average out to zero. These facts can be demonstrated as follows. The potential energy and Hamiltonian (H) of a magnetic moment in a magnetic field, $\vec{B}$ is given by [13]:

$$H = -\vec{\mu} \cdot \vec{B}, \tag{3.2}$$

where $\vec{\mu}$ is the magnetic moment. For a wire loop we know that $\vec{\mu}$ takes the following form:

$$\vec{\mu} = Ia\hat{n}. \tag{3.3}$$

In this equation, I is the current through the loop, a is the area bounded by the loop, and $\hat{n}$ is a unit vector orthogonal to the loop's surface. The magnetic flux Φ through this loop is merely the dot product of the magnetic field, $\vec{B}$ and the area vector $\vec{a}$.

$$\Phi = \vec{B} \cdot \vec{a} = \vec{B} \cdot a\hat{n}. \tag{3.4}$$

Assuming an applied magnetic field of $\vec{B} = B_0 \cos(\omega t)\hat{n}$, we can apply Faraday's law and Lenz's law (see Section 3.2.2) to find that the emf ($\mathcal{E}$) induced in the loop by the changing magnetic field is given by:

$$\mathcal{E} = -\frac{\partial \Phi}{\partial t} = -\frac{\partial \vec{B}}{\partial t} \cdot a\hat{n} = B_0 \sin(\omega t)a. \tag{3.5}$$

To convert this induced emf to an induced current ($I_{induced}$) we simply apply Ohm's law for an AC circuit by dividing by the complex impedance Z.

$$I_{induced} = \frac{\mathcal{E}}{Z}. \tag{3.6}$$

Z is a complex number consisting of a real part equal to the resistance, R, of the wire and an imaginary part consisting of the reactance, X, of the wire.

$$Z = R + iX. \tag{3.7}$$

In our case, the reactance consists entirely of inductive reactance, which is given by the product of the frequency, ω, and the inductance, L. Therefore we can substitute Eq. 3.5 for $\mathcal{E}$ in Eq. 3.6 to find the induced current, $I_{induced}$, as follows:

$$I_{induced} = \frac{\mathcal{E}}{Z} = \frac{\mathcal{E}}{R + i\omega L} = \frac{B_0 \sin(\omega t) a}{R + i\omega L}. \tag{3.8}$$

Next, it is helpful to examine two possible regimes and discuss the impact on the force experienced by the ring. Firstly, let us look at the regime where resistance dominates over the reactance ($R \gg \omega L$). Since R is large with respect to ωL, we neglect this second term in the denominator and find the following:

$$\vec{\mu} = I a \hat{n} = \frac{B_0 \sin(\omega t) a^2 \hat{n}}{R}. \tag{3.9}$$

$$H = -\vec{\mu} \cdot \vec{B} = \frac{-B_0{}^2 \sin(\omega t) \cos(\omega t) a^2}{R}. \tag{3.10}$$

This may look rather uninteresting, but a profound thing has happened. The $\sin(\omega t) \cos(\omega t)$ term will time average to zero, meaning the potential energy H will time average to zero too:

$$< H >= 0. \tag{3.11}$$

If the potential energy is equal to 0, then the force on the ring must equal zero also. This is because force is the gradient of potential. Then in the resistive limit, we have no hope of moving the conducting ring.

However, in the inductive regime, where $\omega L >> R$, we ignore the resistance and set $Z = i\omega L$. The presence of the imaginary number i in the denominator corresponds to a 90 degree phase shift, meaning that I is now proportional to $\cos(\omega t)$. In this case,

$$H = -\vec{\mu} \cdot \vec{B} = \frac{-{B_0}^2 \cos^2(\omega t) a^2}{\omega L}, \tag{3.12}$$

which does not average to 0 over time. Instead, the cosine term will average to $\frac{1}{2}$, giving

$$<H> = -\vec{\mu} \cdot \vec{B} = \frac{-{B_0}^2 a^2}{2\omega L}. \tag{3.13}$$

The gradient of this potential energy is related to the force experienced by the conducting ring. In theory then, we should be able to observe the movement of a conducting circuit when placed in the vicinity of an alternating current in a trace or wire, provided the frequency of the current is high enough that the inductance dominates over the resistance. The frequency where the inductance becomes larger than the resistance is called the cutoff frequency. When operating above this frequency, we can apply forces to conducting rings. With configurations of several wires it may be possible create forces such that local minima in the potential energy are generated and the conducting ring is trapped.

3.1.1 Microring Cutoff Frequency Calculation

Preliminary calculations of microring cutoff frequencies and repulsive forces modelled the ring as a conducting torus. Later iterations modelled the microrings as multi-turn hairpin loops. This second model proved simpler for calculations and for creation of the actual microrings. However, it will be useful to study a rudimentary calculation using the torus model to illustrate the underlying physics of the microring experiment.

For the regime where the self-inductance (L) of the ring dominates the resistance

(R), we require that the inductive reactance is larger than the resistance:

$$\omega L > R. \tag{3.14}$$

Here, ω is the frequency of the applied alternating current. The inductance of a torus was calculated to be:

$$L = \frac{\mu_0 D}{2}(\ln \frac{8D}{d} - \frac{7}{4}), \tag{3.15}$$

where D is the diameter of the ring and d is the cross-sectional thickness of the ring [14]. The resistance of a wire is given by:

$$R = \frac{\rho l}{A}, \tag{3.16}$$

where ρ is the resistivity of the wire material, $l/$ is the length of the wire, and A is the cross-sectional area of the wire. Expressing this equation in terms of the previously defined geometric terms, we find that

$$R = \frac{4\pi D \rho}{\pi d^2} \tag{3.17}$$

Finally, it is simple to substitute Eq. 3.15 and Eq. 3.17 into Eq. 3.14 and solve for the cutoff frequency, ω_0:

$$\omega > \omega_0 = \frac{R}{L} = \frac{8\rho}{\mu_0 d^2(\ln \frac{8D}{d} - \frac{7}{4})}. \tag{3.18}$$

Eq. 3.18 provides the frequency at which inductance becomes dominant and at which we expect to start seeing repulsive forces for a microring of toroidal geometry. Note from the form of this equation that the cutoff frequency is primarily dependent on the cross-sectional diameter of the ring. Smaller rings mandate a higher frequency, since the cutoff frequency, is inversely proportional to d^2. For this reason, the rings constructed so far have been on roughly the milli scale (10^{-3} m) rather than the micro scale (10^{-6} m). A sample calculation with a ring diameter of 10 mm and a thickness

diameter of 2 mm yields a cutoff frequency of 2196 Hz. For actual experiments, it would be ideal to use a frequency that is much higher than the cutoff frequency to guarantee that we are in the inductive regime. However, we are somewhat limited in access to power supplies that can provide both sufficient current to generate a large force and sufficiently high frequency waves to ensure the experiment operates above the cutoff frequency. Experiments conducted with microwave frequencies (1 GHz to 1000 GHz) are well above the cutoff frequencies for torus shaped rings on the scale of a millimeter, as demonstrated by the earlier calculation.

3.1.2 Inductive Microring Force Calculation

We can simplify the force calculations by moving from the toroidal model to one where we approximate our microrings as a thin and narrow hairpin shaped loop [6]. The hairpin ring model is better suited to generating a force from the alternating current (and alternating magnetic field) of a long wire. Moreover, these hairpin loops are easier to create at small scales than toroidal rings. A thin, infinitely long wire carrying a current $I = I_0 sin(\omega t)$ generates the following magnetic field via Ampere's law:

$$\vec{B}(s, t) = \frac{\mu_0 I_0}{2\pi s} \sin(\omega t),\tag{3.19}$$

where s is the cylindrical distance from the wire. A hairpin loop of width D, wire thickness d, and height h placed in this oscillating magnetic field at a distance of s from the wire will experience an emf generated by the changing magnetic flux through its area. This is described as follows:

$$\mathcal{E} = -\int \frac{\partial \vec{B}}{\partial t} \cdot d\vec{a}.\tag{3.20}$$

Next, it will be easiest to see the inductive effects of the ring if we adopt the complex exponential notation for this integration. We can also substitute $e^{i\omega t}$ for $\sin(\omega t)$ since

our choice of trigonometric function is arbitrary. Then,

$$\mathcal{E} = -\int \frac{\partial \vec{B}}{\partial t} \cdot d\vec{a} = -\mu_0 I_0 i\omega e^{i\omega t} \int_d^{D-d} \int_{s+d}^{s+h-d} \frac{1}{2\pi s} ds dz. \tag{3.21}$$

For the case where the inductance is much larger than the resistance (in other words, when $\omega \gg \omega_0$, the result of this integration can be divided by $i\omega L$ to find the induced current in the wire. The inductance for a hairpin loop is given below [6]:

$$L = \frac{\mu_0 D}{\pi} \ln\left(\frac{h-d}{h}\right), \tag{3.22}$$

where again, D is the length of the loop, h is the width of the loop, and d is the cross-sectional diameter of the wire. With this inductance, we find that [6]:

$$I = \frac{-I_0 e^{i\omega t}(D-2d)ln(\frac{s+h-d}{s+d})}{2D\ln\left(\frac{h-d}{h}\right)}. \tag{3.23}$$

We can now use the current equation to find the magnetic dipole moment $(\vec{\mu})$ of the hairpin loop; then, we can dot the real part of this moment with the real part of the magnetic field to find the potential energy of the system:

$$U = -\vec{\mu} \cdot \vec{B} = -I\vec{a} \cdot B = \frac{\mu_0 I_0 \cos^2(\omega t)(D-2d)^2 h \ln\left(\frac{s+h-d}{s+d}\right)}{4\pi s D \ln\left(\frac{h-d}{h}\right)}. \tag{3.24}$$

Finally, we can find the force on the hairpin loop as a function of its distance coordinate, s, from the long wire simply by taking the gradient of the potential:

$$\vec{F}(s) = -\vec{\nabla}U = -\frac{\partial}{\partial s}U(s)\hat{s} \tag{3.25}$$

$$\vec{F}(s) = \frac{\mu_0 I_0^2 \cos^2(\omega t)(D-2d)^2 h}{4\pi D \ln\left(\frac{h-d}{h}\right)}\left[\frac{h-2d}{s(s+d)(s+h-d)} + \frac{\ln\left(\frac{s+h-d}{s+d}\right)}{s^2}\right]\hat{s}. \tag{3.26}$$

Preliminary calculations show the magnitude of the force for the given experimental setup will be 1×10^{-4} N. Note that this calculation is for a single turn loop. A hairpin loop with several turns will have a higher inductance. Specifically, a loop of N turns will have an inductance of NL, where L is the inductance of the single-turn

loop. The final force remains unaffected by the extra factor of N in the denominator, however, since the magnetic moment of the ring is also scaled upwards by a factor of N. This informed the choice to use a multi-loop hairpin since the force is not decreased but the cutoff frequency is scaled down by a factor of N.

3.2 Experimental Design and Results

The experimental setup for detecting the force on the multi-turn hairpin loop is the following. A long copper wire was fixed vertically and held taught. A multi-turn hairpin loop was positioned so that the loop was parallel with the long copper wire and brought close to the main wire. Then, a sinusoidal current with a frequency of 1.8 kHz and a magnitude of 2.0 A was applied to the copper wire using a function generator and power supply. This experimental setup is shown in Fig. 3.1. Next, the apparatus was observed for signs of movement. So far, no movement has been observed but experiments to verify the inductive properties of the loop are ongoing. Experiments conducted at the highest possible frequency of 10 kHz still yielded no net movement of the microring.

There are several possible explanations for the lack of observed force. First, from the form of Eq. 3.26, the force on the ring depends on several variables. Larger applied current (increase I_0), larger ring diameter (increase D), thinner wire diameter (decrease d), and shorter distances from the vertical wire (decrease s) will all increase the force on the conducting ring. It may also be that the predicted force of roughly 1×10^{-4} N was applied to the ring, but was so small as to be undetectable. The final possibility is that Eq. 3.26 is not valid at all. This can be the case if the applied frequency is not larger than the cutoff frequency, in which case we expect no net force on the ring.
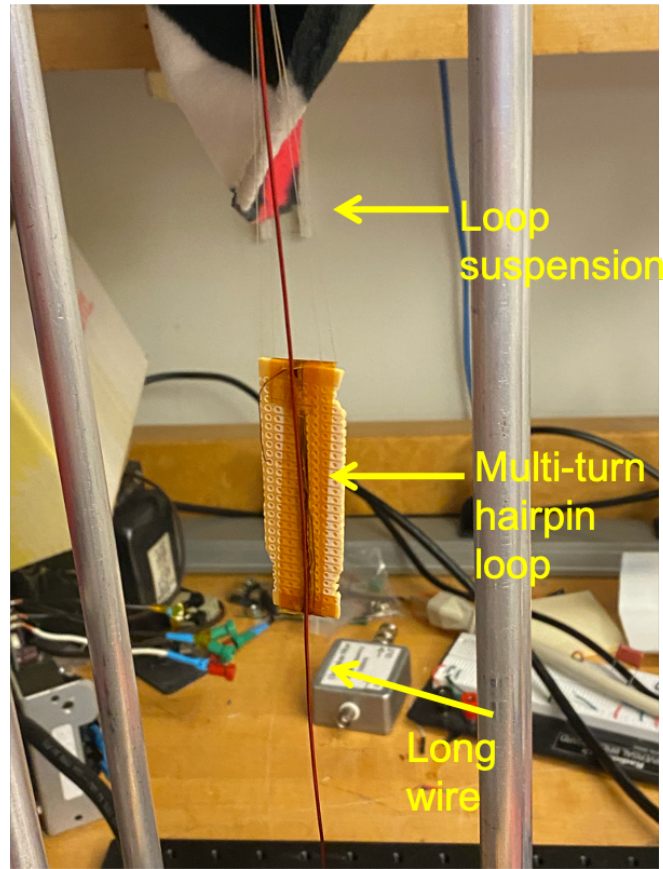
Figure 3.1: The microring experiment apparatus is shown on the top. The multi-loop hairpin is suspended such that it is parallel to a vertical wire which carries an AC current generated by a power supply and a function generator

With no force observed, it was unclear if the experiment was operating in the inductive regime above the cutoff frequency. The induced current was investigated using a multi-turn pickup coil placed within a solenoid to better understand the underlying physics and to make a rough estimate of the cutoff frequency. The experimental setup for the cutoff frequency experiment is shown in Fig. 3.2.

Figure 3.2: The cutoff frequency measurement experimental setup is shown above. Alternating current applied to the solenoid generates a magnetic field that oscillates inside of the solenoid, which induces a current in the pickup coil. These currents are then measured and their relative phase shift compared to find the cutoff frequency

The frequency of the AC current through the solenoid was varied between 40 Hz and 10 kHz and the induced current in the pickup coil and the applied c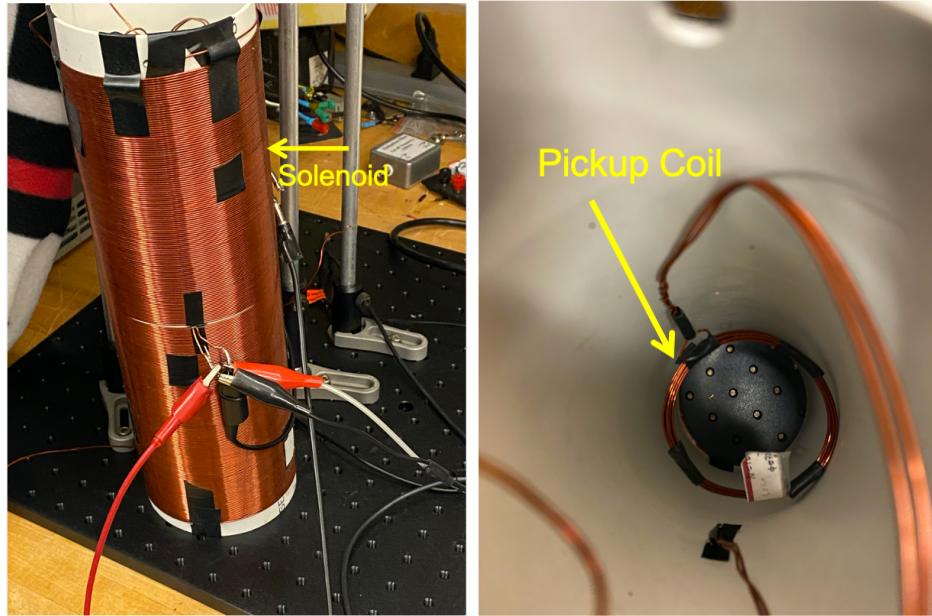urrent through the solenoid were measured and viewed on an oscilloscope. A phase shift of roughly 90 degrees between the two current signals was observed at applied frequencies between 41.1 Hz and 1.1 kHz. This indicated that resistance was dominating over inductance, and therefore there would be no net force on the pickup coil. Since the currents are 90 degrees out of phase, the force equation will average out to zero over time. However, at 10.35 kHz, we observed a phase shift of 135 degrees between the two sinusoidal waves. This indicates a shift towards the inductive regime, where there will be a non-zero net force. Ideally, the actual frequency will be much larger than 10 kHz to ensure that we operate entirely in the inductive regime. In the case where the inductance is very large and resistance is negligible, the phase shift should be 180

degrees. The observed phase shift at various frequencies is shown in Fig. 3.3.
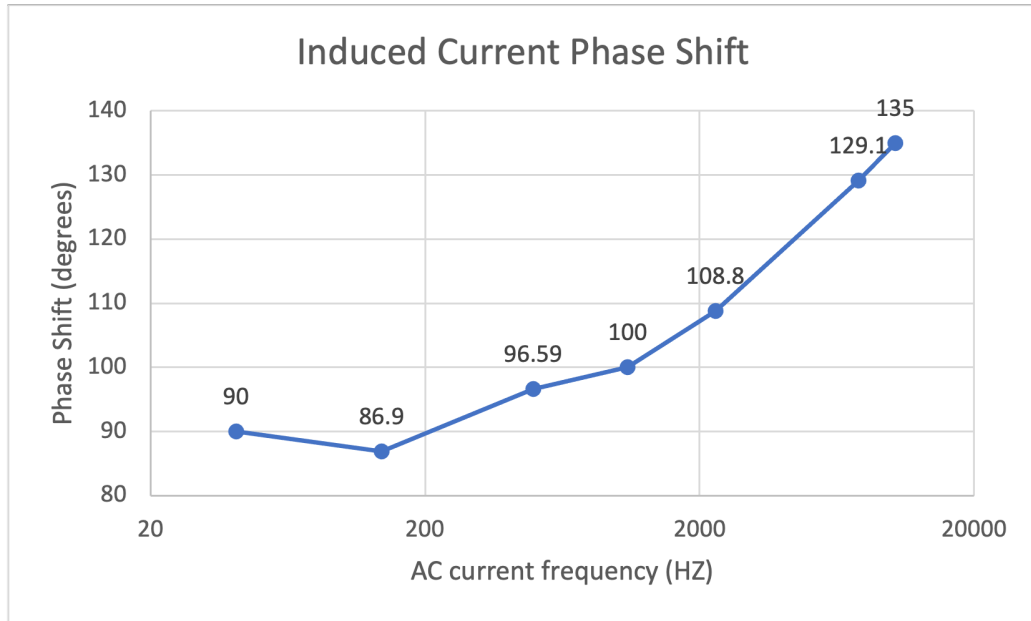
Figure 3.3: The phase shift experimental data. At low frequencies, the phase shift is roughly 90 degrees while at 10 kHz there is a phase shift of 135 degrees. This indicates that inductive reactance becomes larger than resistance around 10 kHz.

The experimentally measured phase shift between the solenoid current and the induced pickup coil current is shown at two frequencies in Fig. 3.4. At 194.7 Hz there is a phase shift of 90 degrees while at 9.4 kHz there is a phase shift of 135 degrees.

Figure 3.4: Oscilloscope screenshots of the solenoid current (purple) and the induced pickup coil (yellow) recorded at low (left) and high (right) frequencies respectively. As frequency increases, the phase shift increases from 90 degrees to 135 degrees.

Chapter 4

Atom Chip Substrate Development

As part of an ongoing, related project to create atom chips for Bose-Einstein condensate microwave interferometry, I assisted with the early steps for preparing copper substrates for future microwave atom chips. These small copper plates (3 cm x 3 cm, 2 mm thick) must 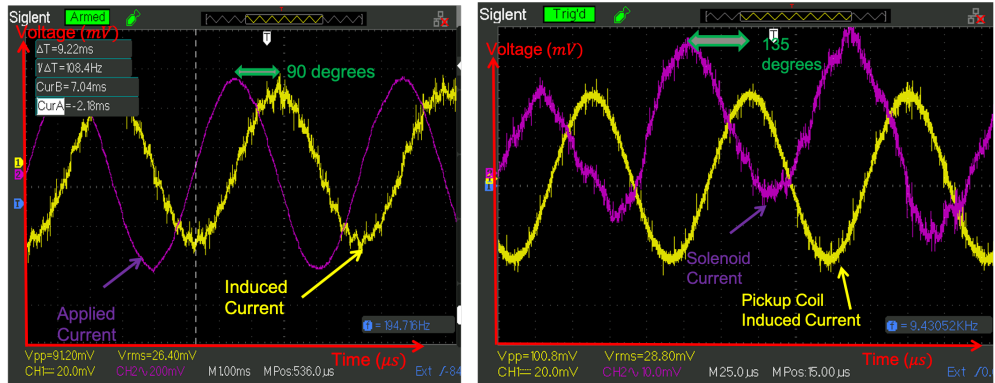be made very flat and also smooth in preparation for commercial coating with aluminum nitride (50 mum thick). This aluminum nitride serves as the dielectric substrate that separates conducting traces from the ground plane (just as FR4 did in the microsphere experiments).

4.1   Surface Profile Characterization

The first step of this project involved the characterization of the surface profile of several 3 cm x 3 cm copper plates using the Profilm 3D Surface Profiler and Dektak 3ST Surface Profiler at W&M's Applied Research Center CoreLabs. The Profilm 3D Surface Profiler was used to measure height differences across a 10 mm x 10 mm section of the plate; however, we are interested in the overall surface profile of the copper plate. Large height variations of the height profile can make it much harder to properly apply microwaves to the atom chip. Better luck was had with the Dektak 3ST Surface Profiler. A copper sample is shown on the measurement platform of the Dektak instrument in Fig. 4.1.
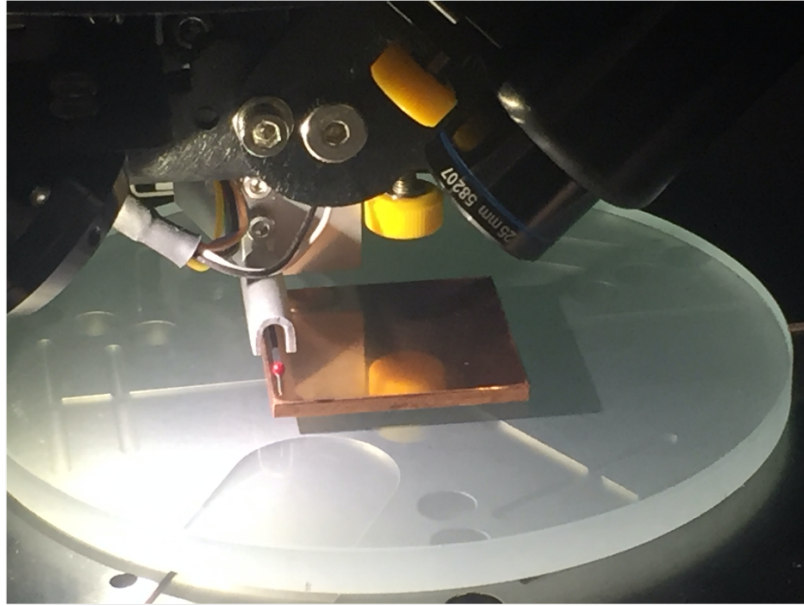
Figure 4.1: A 3x3 *cm* copper plate in the Dektak instrument for surface profiling.

This instrument was used to gather data on the height of the chip across its entire length by dragging a tiny needle across the surface of the plate. Moreover, I was able to generate an overall surface profile by interpolating several height profiles across the width of the square. The final profile resembles that of a shield laid flat on the ground. The plate is tallest in the center, while the edges and the corners are lower. The total height difference is less than 6 microns across the copper substrate (3 cm x 3 cm, 2 mm thick). The profilometer results are shown in Fig. 4.2.

Figure 4.2: The interpolated surface profile of the polished copper square. The square is fairly flat in the center, while the edges are 2 microns lower than the center and the corners are 6 microns lower. The graphs on the right show an x and y profile for a given location on the plate.

4.2 Copper Square Polishing

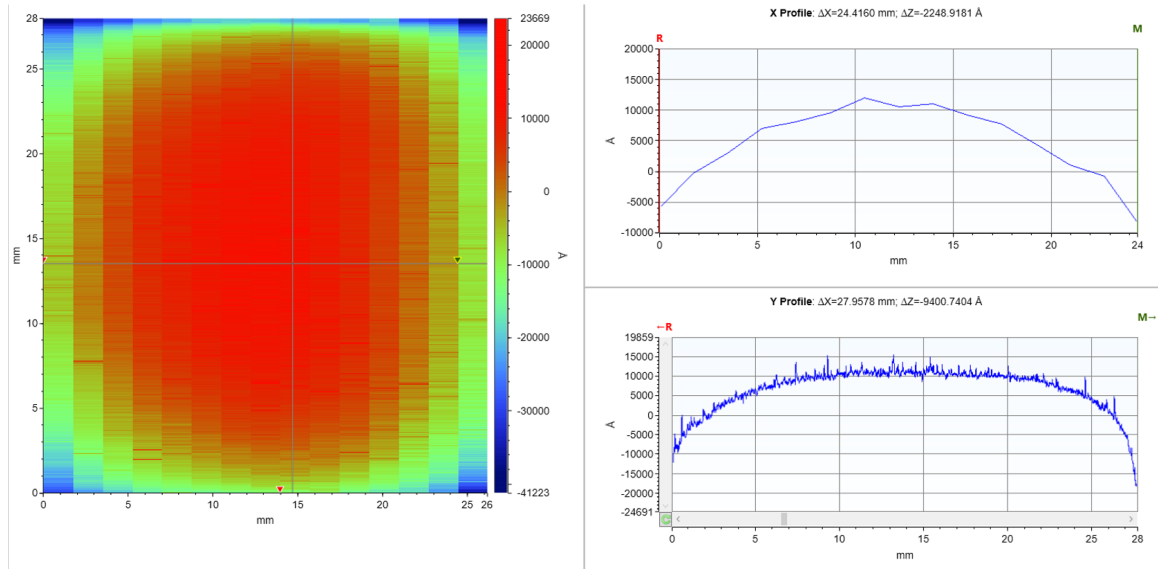I used sandpaper to achieve a more even and smooth surface for the future atom chip. This involved using progressively higher grain sand paper on the copper plate. For those who will continue with the polishing process in the future, I used the following sandpaper grits in succesion: P200, P220, P240, P320, P400, P600, P800, P1000, P1200, P1500, P2000, P2500, P3000, P5000, and P7000. The sanding procedure involved rubbing the copper sample against the sandpaper in a figure eight motion until the largest scratches had disappeared. I would then slide the copper sample perpendicular to any larger scratches. Before moving to the next grit level, I was careful to rinse the copper square with soapy water to remove any excess copper material or grit from the sandpaper. I also shook off each sheet of sandpaper before use. These two steps are highly important; without them, you may accidentally create

large scratches when you move to the next grit size. This can set back hours of work. An example of the copper square before and after this polishing procedure can be seen in Fig. 4.3
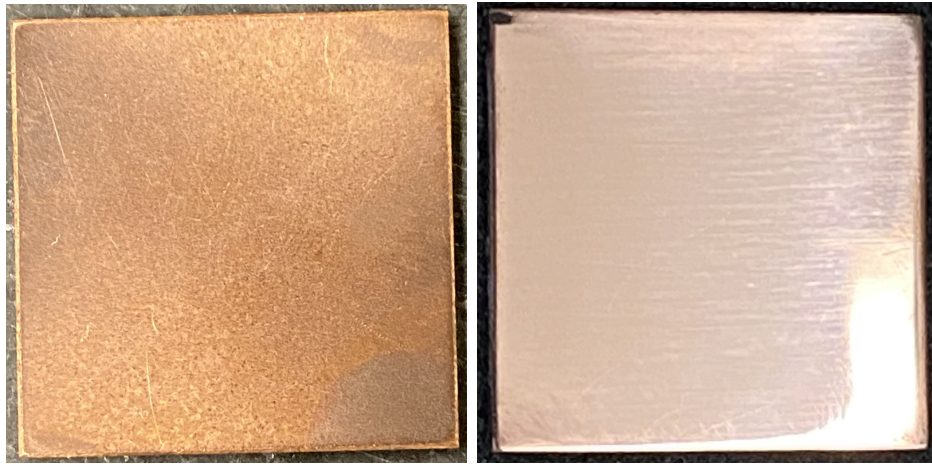
Figure 4.3: The copper plate, before and after polishing procedure

A buff wheel was also used to polish a copper sample. This improved local smoothness, but the overall surface profile flatness was drastically worse. The height difference across the copper sample increased to 60 microns, as shown in Fig. 4.4. This is likely because the buff wheel would round down the edges of the chip. In conclusion, future copper square polishing should avoid use of the buff wheel and instead aim for a manual sanding procedure.

Figure 4.4: The interpolated surface profile of a copper square polished using the new polishing procedure and the buff wheel. The square is reasonably flat in the center, but the edges are rounded down so that he overall height variation is 60 microns across the surface. The graphs on the right show an x and y profile for a given point on the plate.

4.2.1 Force Calculation for 54 Micron Atom Chip

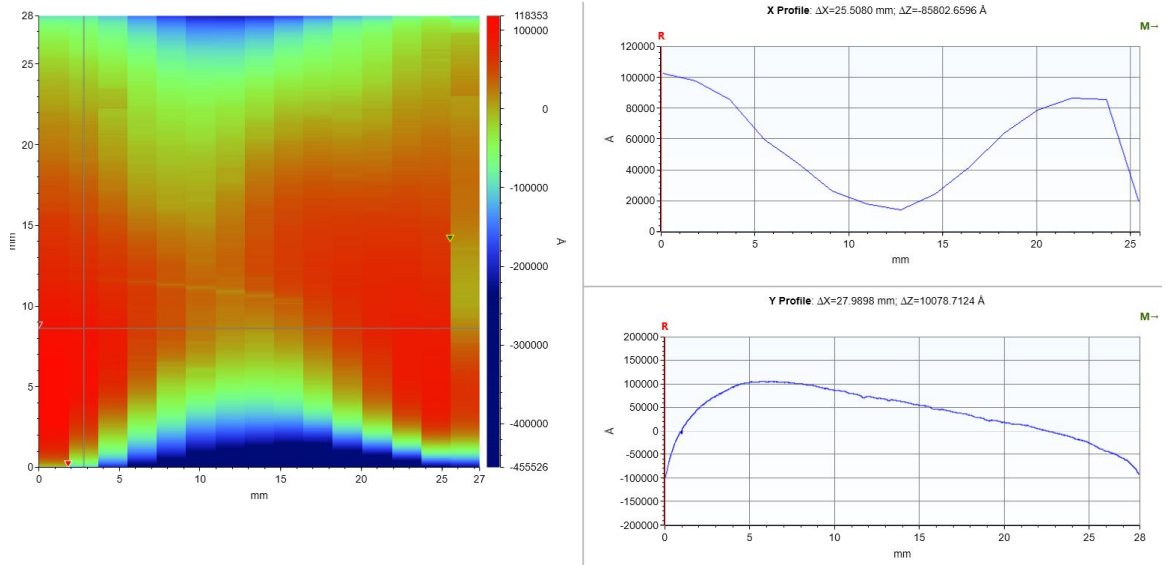I repeated the earlier FEKO simulations but with the dimensions of the planned future atom chips. These simulations yielded the electric field generated for 10 frequencies in the microwave range (1 GHz to 10 GHz). The electric field for a 1 GHz simulation was plugged into Eq. 2.1 to find the acceleration experienced by polyethylene microspheres in the vicinity of the atom chip. In this simulation, the microspheres are 8.9 microns above the 54 micron trace, which is powered by a 20 W microwave amplifier. The microspheres are surrounded by air. The resultant acceleration is shown in Fig. 4.5. A maximum acceleration of 60 $\frac{m}{s^2}$ is predicted.

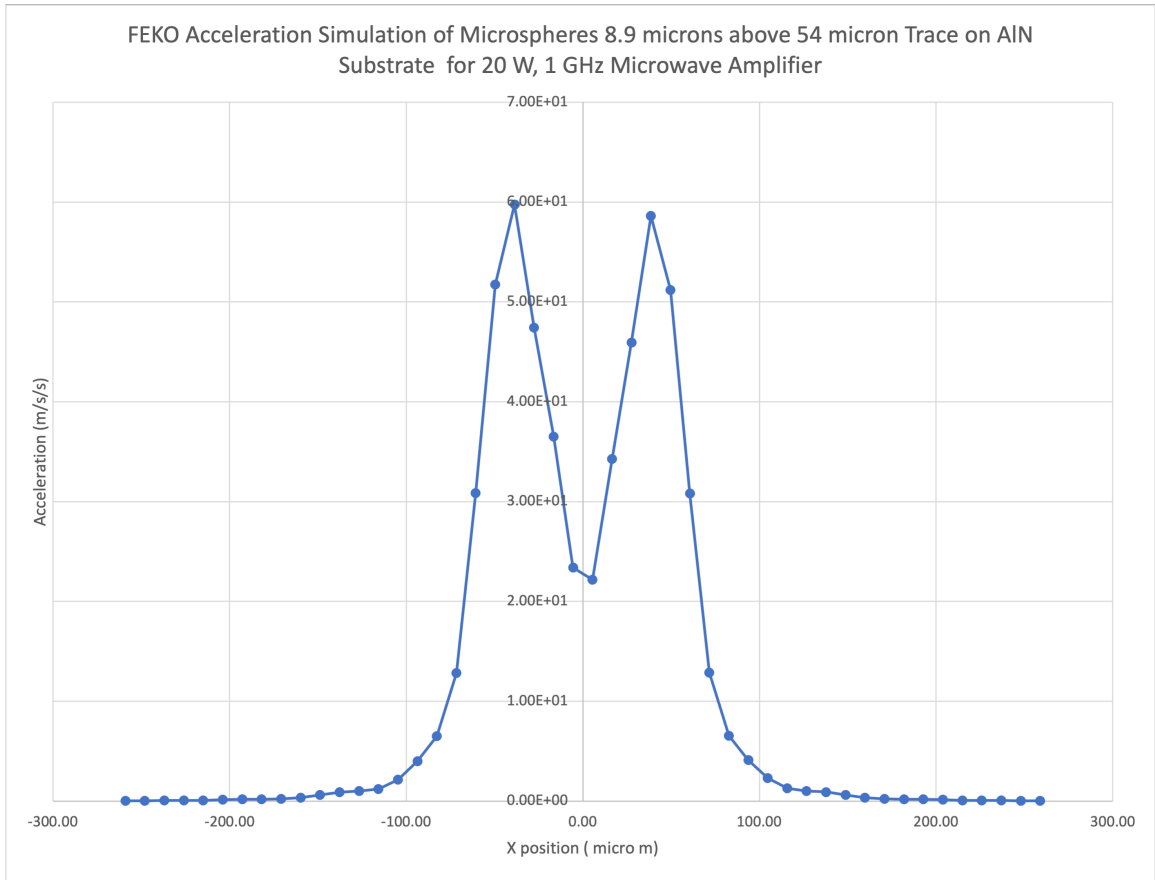Figure 4.5: The acceleration experienced by a polyethylene microsphere 8.9 microns above the atom chip as a function of the microsphere's position. The medium for the microsphere is air.

Future work will involve using these simulations to calculate the force on atoms near traces and to evaluate ultra-cold atom trapping using microwaves. The force on ultra-cold atoms will depend on the magnetic field, rather than the electric field.

Chapter 5

Conclusion/Outlook

In summary, this thesis has described research to develop mechanisms to apply electric forces on dielectric microspheres and magnetic forces on conducting microrings. The research successfully constructed an apparatus that observed electrostatic forces generating motion of microspheres suspended in dielectric liquid. The observed movement did not agree with initial theories. The research conducted also investigated the magnetic force on conducting microrings and the theoretical cutoff frequencies and forces experienced by various microring geometries. Experiments were also conducted to observe the force on a microring in a changing magnetic field and to investigate the relationship between frequency and phase shift between the induced current and the long wire current. Using a pick up coil and solenoid, the cutoff frequency at which inductance dominates was measured, confirming the underlying physics for future experiments. Progress was also made towards the development of atom chip substrates for future microwave experiments. The research involved developing experimental methods to characterize the surface profile and flatness of atom chip substrates and creation of new processes for the polishing of copper substrates.

The disagreement between theory and experiment with regards to electrostatic microsphere movement remains open and needs to be reconciled. It is not clear why the dielectric oils act as weak-field seekers and why the microspheres largely

remain stationary. The two most likely explanations are that experiments must be conducted at higher frequencies for the original force equation to be valid and the need for higher electric field gradients to overcome competing Coulombic and drag effects. Future experiments may occur to investigate this discrepancy. For example, future students might repeat the microsphere experiments for high frequencies rather than DC current or attempt to build smaller microstrip traces that will produce sharper gradients.

5.1   Possible Future Microwave Experiments

Future projects building off of this thesis may aim to use microwave electronics. This microwave portion of such a project will aim to use a microwave lattice to generate axial forces along the traces by delivering counter-propagating microwaves from either end of the trace to create a standing wave. If the microwaves have the same frequency and amplitude; varying their relative phase will shift the nodes of the standing wave along the microstrip axis. Therefore, varying the relative phase of the microwaves can be used to shift the trapped micro-particles along the traces axis [1]. The same microwave lattice could be used to create a movable magnetic field minimum that will be used to translate trapped microrings axially along the trace axis. Figure 5.1 shows a three trace geometry for generating a microwave magnetic field minimum for transverse trapping of conducting microrings. At high frequencies, the microrings are expected to be dynamically diamagnetic.
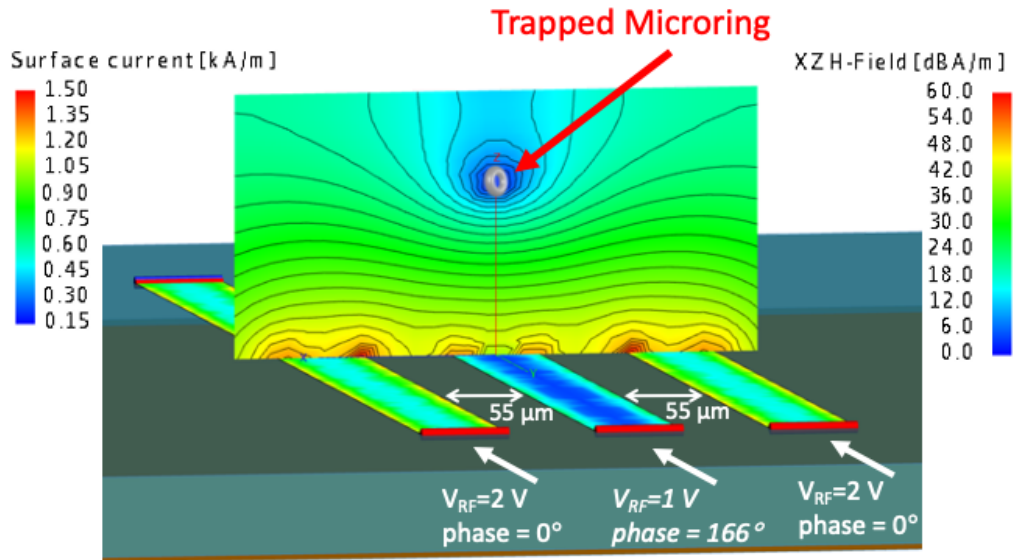
Figure 5.1: Figure adapted from original diagram by S. Aubin. Transverse trapping of a microring using the magnetic microwave near field generated by three microstrip transmission lines at 7 GHz on an AlN substrate (simulated with FEKO software).

Future experiments that build off this thesis could aim to introduce microwave electronics to translate or levitate microrings as described above. Introduction of multi-trace configurations may also enable the trapping of microspheres [1].

Appendix A

Electron Beam Analysis

A.1 Gaussian Beam Analysis Code

What follows is the Python code which analyzes the electron beam data. It takes the .tif image of the beam gathered with the CCD camera and extracts each pixel's brightness. The brightness of each pixel is stored in an array. The size of the array corresponds to the dimensions of the camera (960 x 1280 pixels). Then, the values in each column are summed together, leaving just a horizontal brightness profile (now a 1 by 1280 array). This profile reveals a Gaussian distribution, as expected. Finally, the code calculates the full width at half maximum of the beam.

```
/************************************************************/

/*   Andrew J Beling   */
%matplotlib inline
import numpy as np
import scipy as sp
import matplotlib.pyplot as plt
import math
import numpy.matlib as ml
import scipy.integrate as ig
import scipy.interpolate as ip
import scipy.optimize as op
import PIL
from PIL import Image
np.set_printoptions(threshold=1000)
#threshold=sys.maxsize

from google.colab import files
from io import BytesIO
from PIL import Image

uploaded = files.upload()
img = Image.open(BytesIO(uploaded['ebeam_spot_2020-10-16_picA.tif']))
img.show()
img_arr = np.array(img)
```

```python
img_arr.shape

img_arr.dtype

img_arr
#print(img_arr[0][0])

gauss_arr = np.mean(img_arr, axis=0)

gauss_arr.shape

plt.plot(gauss_arr)
plt.xlim(500, 800)
plt.xlabel("position (pixels)")
plt.ylabel("intensity sum (a.u.)")

pixel = np.arange(0,1280)
gauss_interp = ip.InterpolatedUnivariateSpline(pixel,gauss_arr)
t2 = np.linspace(0,1280,15000)
plt.plot(t2, gauss_interp(t2))
plt.xlim(500, 800)
plt.xlabel("position (pixels)")
plt.ylabel("intensity sum (a.u.)")

max_y = max(gauss_arr)
xs = [x for x in range(1280) if gauss_arr[x] > max_y/2.0]
FWHM_pixel = (max(xs)-min(xs))
print(FWHM_pixel)

pixel_density = 4.615
FWHM = FWHM_pixel * pixel_density
print(FWHM)
```

Bibliography

[1] Chloe Lewelling. Electromagnetic simulations of microwave trapping structures. *Bachelor of Science Thesis, William and Mary*, 2018.

[2] Arthur Ashkin. Acceleration and trapping of particles by radiation pressure. *Physical review letters*, 24(4):156, 1970.

[3] Asuka Nakano and Alexandra Ros. Protein dielectrophoresis: advances, challenges, and applications. *Electrophoresis*, 34(7):1085–1096, 2013.

[4] Ralph Hölzel and Ronald Pethig. Protein dielectrophoresis: I. status of experiments and an empirical theory. *Micromachines*, 11(5):533, 2020.

[5] Fernanda Camacho-Alanis and Alexandra Ros. Protein dielectrophoresis and the link to dielectric properties. *Bioanalysis*, 7(3):353–371, 2015.

[6] David J Griffiths. Introduction to electrodynamics, 2005.

[7] Seth Aubin. Private Communication, 2020.

[8] Kameron Sullivan. Simulation and prototype construction of microwave atom chip components. *Bachelor of Science Thesis, William and Mary*, 2019.

[9] Zhaolin Lu, Janusz A Murakowski, Christopher A Schuetz, Shouyuan Shi, Garrett J Schneider, Jesse P Samluk, and Dennis W Prather. Perfect lens makes a perfect trap. *Optics express*, 14(6):2228–2235, 2006.

[10] Joseph Louis Van Meter. A study of microstrip transmission line parameters utilizing image theory. *University of Missouri–Rolla Thesis, 1970*, 1970.

[11] L Benguigui and IJ Lin. The dielectrophoresis force. *American Journal of Physics*, 54(5):447–450, 1986.

[12] Yelena Lipovetskaya. Electrostatic charge on microspheres and microparticles, Feb 2017.

[13] David J Griffiths. Introduction to quantum mechanics, 2017.

[14] SY Mak and K Young. Determination of the self-inductance of a metal ring. *Physics Education*, 21(2):111, 1986.